Robotica (2014) volume 32, pp. 447–466. © Cambridge University Press 2013
doi:10.1017/S0263574713000714

Comparison of two calibration methods for a small industrial robot based on an optical CMM and a laser tracker

Albert Nubiola, Mohamed Slamani, Ahmed Joubair and Ilian A. Bonev*

École de Technologie Supérieure, Montreal, Quebec, Canada

(Accepted June 17, 2013. First published online: August 9, 2013)

SUMMARY
The absolute accuracy of a small industrial robot is improved using a 30-parameter calibration model. The error model takes into account a full kinematic calibration and five compliance parameters related to the stiffness in joints 2, 3, 4, 5, and 6. The linearization of the Jacobian is performed to iteratively find the modeled error parameters. Two coordinate measurement systems are used independently: a laser tracker and an optical CMM. An optimized end-effector is developed specifically for each measurement system. The robot is calibrated using fewer than 50 configurations and the calibration efficiency validated in 1000 configurations using either the laser tracker or the optical CMM. A telescopic ballbar is also used for validation. The results show that the optical CMM yields slightly better results, even when used with the simple triangular plate end-effector that was developed mainly for the laser tracker.

KEYWORDS: Robot calibration; Robot identification; Industrial robots; Accuracy; Metrology; Optical CMM; Laser tracker; Ballbar.

1. Introduction

It is well known that the accuracy of an industrial robot can be improved through a process known as *robot calibration*.[1] The first step in this process is to choose a theoretical model that is closer to reality than the nominal model used in the robot controller (e.g., the wrist axes are no longer concurrent and the gearboxes are flexible in the new model). The parameters of this model are then identified by measuring the *complete pose* or *partial pose* of the robot end-effector in a set of *calibration configurations*. In practice, the most critical issue is the choice of measurement system, as the latter determines the efficiency and cost of the robot calibration process.

The identification process can be performed using a wide range of commercially available or custom-designed measurement tools, such as a touch probe and a reference artifact,[2,3] a telescopic ballbar,[4,5] a small-range 3D (position) measurement device, such as a camera-based system[6] and acoustic sensors,[7] a large-range 3D measurement device (such as a laser tracker[8–11] or CMM[4,12,13]), and a 6D (pose) measurement device, such as a camera-based system[8,9,15] or a laser tracker with a 6D probe.[14]

To the best of our knowledge, most industrial robot manufacturers who offer calibration as an option use either a laser tracker (one manufactured by Leica, in the case of ABB and FANUC) or a 6D optical CMM (Nikon Metrology's K-series optical CMM, in the case of KUKA). Furthermore, at least two commercial robot calibration software packages exist, based on 3D or 6D measurement data: DynaCal from Dynalog, and Rocal from Nikon Metrology (both companies based in the United States).

* Corresponding author. E-mail: ilian.bonev@etsmtl.ca

In practice, two types of commercially available position/pose measurement tools can be used for calibrating industrial robots: laser trackers (from Leica, FARO, or API) and optical CMMs (from Nikon Metrology, Northern Digital, Metronor, Geodetic Systems, AICON, GOM, or Creaform). Laser trackers are more accurate and have a very large measurement range, but they are highly sensitive to the ambient conditions (e.g., the air currents present in factory hangars) and are extremely expensive (from at least $100,000 US to nearly $200,000 US or more). Laser trackers generally measure the 3D coordinates of a single point at a time, but they can also be used to measure the complete pose of the robot end-effector in static conditions, by measuring three spherically mounted reflectors (SMRs), or, in dynamic conditions, by using a special 6D probe for measuring. However, at each moment, a laser tracker measures the position or pose of a single body relative to its own reference frame. Therefore, vibrations of the factory floor can significantly decrease the accuracy to which the position or pose of the robot end-effector is measured with respect to the robot base frame.

In contrast, optical CMMs can measure the pose of the robot end-effector dynamically (i.e., at frequencies of 30 Hz or more) with respect to its base. Their measurement volume is smaller than that of laser trackers and they are slightly less accurate (though probably not in real factory conditions), but they are much less expensive and easier to use. Furthermore, optical CMMs can also be used to correct the pose of the end-effector iteratively, as is currently done by Nikon Metrology's Adaptive Robot Control software in conjunction with their K-series optical CMMs.

Some optical CMMs (e.g., those from Nikon Metrology and Northern Digital) use *active targets*, which are basically infrared light-emitting diodes emitting light at prescribed frequencies. Active targets are relatively expensive and cumbersome, but have the advantage of being easily identifiable (targets are illuminated one at a time) and not sensitive to external light conditions. Other systems, such as Creaform's C-Track, use *passive targets*, which are basically small circular stickers covered with retroreflective material and costing no more than a few cents each. The main advantage of passive targets is that one can use plenty of them to build a spatial artifact, the pose of which can be measured with the optical CMM in virtually any orientation.

What motivated this work is the question of whether or not an optical CMM that can measure the pose of a robot end-effector in any orientation is as efficient as a laser tracker in calibrating industrial robots, even in perfect laboratory conditions (where laser trackers have the advantage). Of course, a laser tracker can also be used to measure the pose of an object in any orientation, but this would either require too much operator intervention during the measurement process, or an artifact with dozens of SMRs that would cost thousands of dollars to manufacture. Note that there are commercial 6D tracking devices that can be used in conjunction with a laser tracker (e.g., Leica's T-Mac or API's SmartTRACK); however, these are not only very expensive, but also function in a rather limited orientation range.[14] In contrast, developing such a spatial artifact out of passive reflectors would add only a small fraction to the cost of an optical CMM.

We believe that our work here is the first to compare the efficiency of a laser tracker in industrial robot calibration and that of a commercially available optical CMM. In particular, we use a FARO laser tracker in conjunction with three SMRs and Creaform's C-Track (launched in 2010), in conjunction with two custom-designed artifacts. The robot to be calibrated is an ABB IRB 120. This model is ABB's smallest industrial robot, launched in 2009, and is one of the few robots for which ABB does not offer factory calibration. We used a standard calibration model that takes into account all 25 kinematic parameters, as well as five compliance parameters, for the harmonic gearboxes of axes 2, 3, 4, 5, and 6. These 30 parameters are identified by linearization of the model in fewer than 50 calibration poses obtained through an observability study. Finally, the efficiency of the robot calibration process in each of three different setups is validated with a Renishaw telescopic ballbar.

The three experimental setups used are described in the next section. Section 3 describes the robot kinematic model, while Section 4 shows the sources of nongeometric errors and summarizes the nonkinematic model. The calibration procedure is described in Section 5, and the results are given in Section 6. Our conclusions are presented in Section 7.

2. Experimental Setups

Figure 1 shows the installation used for calibrating the ABB IRB120 robot with a FARO laser tracker ION. Our laser tracker has only the ADM option, which means that it is slightly less accurate (compared to when using the interferometry option) but allows full automation of measurements, as

https://doi.org/10.1017/S0263574713000714 Published online by Cambridge University Press

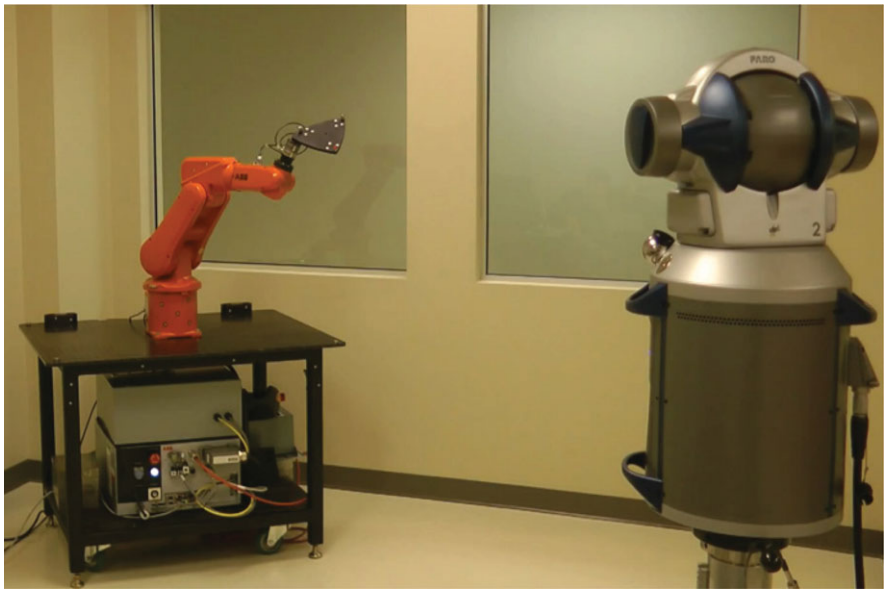

Fig. 1. (Colour online) Experimental setup for calibrating the robot with FARO's ION laser tracker.

the laser beam can be redirected from one SMR to the other without the need for manual initialization. The robot was fixed to a heavy steel table that was immobilized with about 200 kg of additional load on its lower shelf. An SMR fixed on the table was measured using the laser tracker in various robot configurations, and it was shown that the table top does not deflect by more than $\pm$ 0.010 mm at the SMR's location for the speeds and accelerations used. A special triangular artifact with three 0.5″ SMRs (and nine retroreflective self-adhesive targets on each planar face) was used, and will be described in Section 2.1.

According to the specifications of our laser tracker, its typical accuracy when measuring the length of a 2.3 m horizontal scale bar at a distance of 2 m is 0.022 mm. According to our own tests, the largest error when measuring the length of a 1 m scale bar mounted on the end-effector of our robot and located at various places within the robot workspace is about 0.060 mm (the mean error being only 0.035 mm). The laser tracker was not moved from the position depicted in Fig. 1 at any time during measurement.

Figure 2(a) shows the installation used for calibrating the robot with Creaform's C-Track and the same triangular artifact. Figure 2(b) shows the fifteen retroreflective self-adhesive targets that were attached to the base of the robot. All measurements with the C-Track (with both artifacts) were taken relative to the robot's base (unlike the case with the laser tracker). The device was not moved from the position depicted in Fig. 2(a) at any time during measurement (with both the triangular and the spatial artifacts).

The C-Track comes with a special hand-held planar artifact, called the HandyPROBE, which has a rigid probe. The HandyPROBE is used for measuring 3D coordinates, and its volumetric accuracy is 0.075 mm, as per ASME standard B89.4.22. Our own tests showed that the largest error when measuring the length of a 0.5 m scale bar using the HandyPROBE was about 0.065 mm.

The C-Track model used for the tests is the 780, with a measurement volume of 7.8 m^3. However, we calibrated it in a volume of 3.4 m^3, which was enough for our tests. The accuracy recorded by the C-Track's software after completion of the calibration procedure with a special 1 m scale bar was 0.040 mm.

Figure 3 shows a close-up of the installation used for calibrating the robot with the C-Track and the spatial artifact described in Section 2.2.

All measurements were performed in a relatively small laboratory at temperatures varying between 22.5 and 23.5°C. The C-Track, the laser tracker, and the robot were controlled by MATLAB, via Ethernet LAN. Thus, the procedure for taking measures is fully automated and requires no manual intervention (e.g., for reorienting the SMRs or moving the tool-changer's two air hoses). The position

https://doi.org/10.1017/S0263574713000714 Published online by Cambridge University Press

(a)

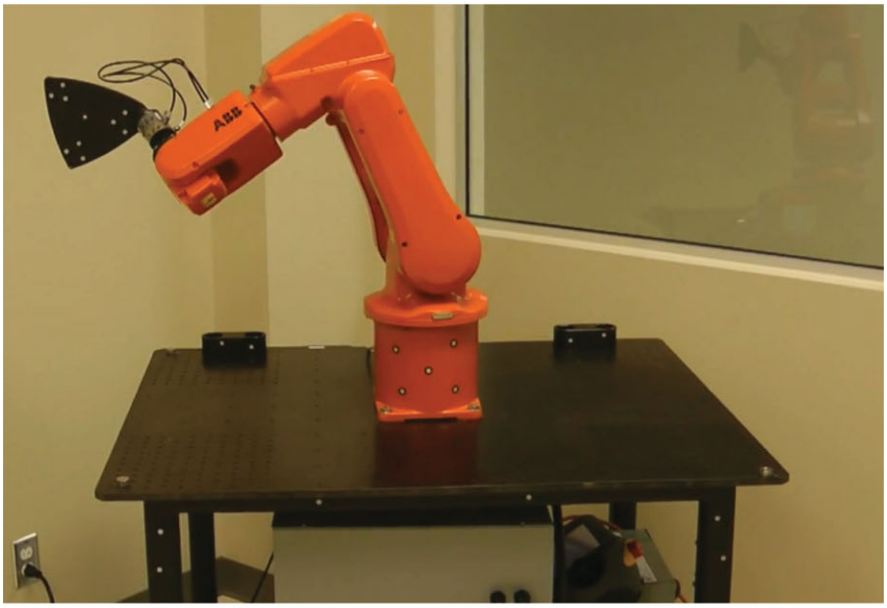

(b)

Fig. 2. (Colour online) Experimental setup for calibrating the robot with Creaform's C-Track and the triangular artifact. (a) Overall setup. (b) Close-up showing the back side of the triangular artifact and the 15 retroreflective targets on the robot's base.

commands sent to the robot are the joint values (i.e., we send *jointtargets* and use the RAPID instruction *MoveAbsJ*).

In each of the three setups, the range of measurable end-effector orientations is obviously different. To take full advantage of each setup, any pose can be a candidate for the identification or the validation phase, as long as it is measurable (with the laser tracker in the first setup, and the C-Track in the second and third setups). In the first setup, the SMRs are orientated outward (see Fig. 1), and the only end-effector orientations used are those in which the $\pm 30^{\circ}$ visibility cone of at least one of the SMRs covers the laser tracker. In the second setup, the angle between the normal to the planar

https://doi.org/10.1017/S0263574713000714 Published online by Cambridge University Press

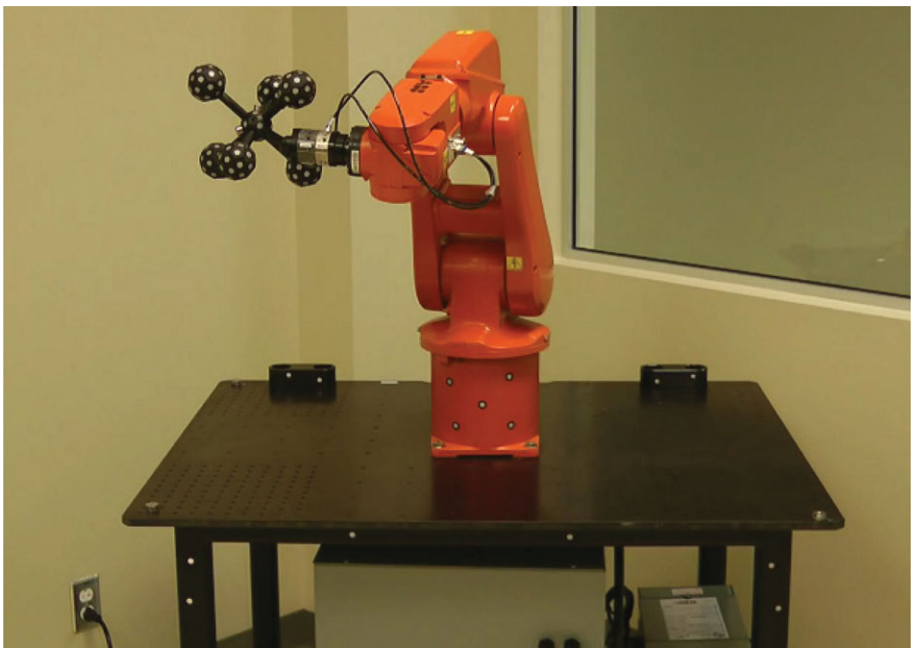

Fig. 3. (Colour online) Experimental setup for calibrating the robot with Creaform's C-Track and the spatial artifact.

surface of the triangular artifact and the line of sight of the C-Track is limited to 15° (both sides of the artifact are used). In the third setup, there are no limits to the orientation of the robot end-effector. However, because the robot arm partially hides the artifacts in some robot configurations, a condition is imposed such that at least nine retroreflective targets from the triangular artifact are seen by the C-Track and 20 from the spatial artifact.

Note that, initially, we also considered a fourth case in which the position of one of three SMRs mounted on the spatial artifact was measured with the laser tracker. However, this fourth case was promptly discarded, since there is obviously no advantage of using the spatial artifact with a laser tracker.

A video showing the experiments described in this paper can be seen at http://youtu.be/i0ztjX0jlSU.

2.1. Triangular artifact

The triangular artifact (Fig. 1) is made of steel and holds three magnetic nests for 0.5″ spheres (SMRs or one end of Renishaw's telescopic ballbar). The distance between the centers of these nests is 150 mm. One of the centers (nest 1) lies on axis 6 of the robot, about 125 mm away from the robot tool flange *xy* plane, another (nest 3) lies in the plane passing through the first center and normal to axis 6, approximately 150 mm away from this axis, and the last one (nest 2) is about 115 mm away from axis 6 and about 215 mm away from the tool flange *xy* plane. Nine retroreflective self-adhesive targets are attached to each side of the tool, as shown in Figs. 2(b) and 4.

Creaform's MaxSHOT 3D photogrammetry system was used to acquire the position of all 18 retroreflective targets with respect to a common reference frame, located in the centroid of all targets. The positions of the centers of the three magnetic nests with respect to this reference frame are measured using the HandyPROBE.

The triangular artifact is mounted on an ATI QC-5 tool changer, and along with the three magnetic nests, weighs approximately 2.4 kg. The master side of the tool changer weighs an additional 0.3 kg, so the complete end-effector weighs about 2.7 kg, the robot rated payload being 3 kg. The coordinates of the center of gravity of the complete end-effector are approximately {50 mm, 25 mm, 100 mm} with respect to the robot flange reference frame, according to the CAD model of the end-effector.

https://doi.org/10.1017/S0263574713000714 Published online by Cambridge University Press

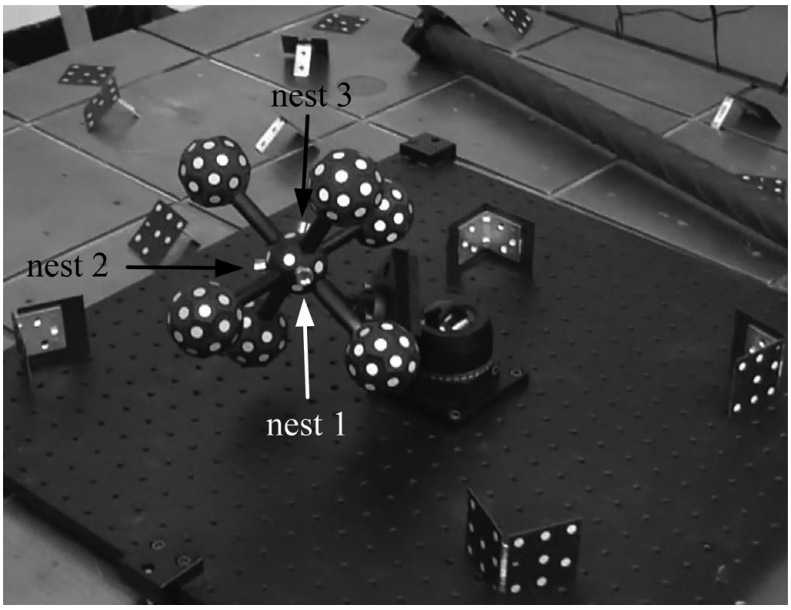

Fig. 4. The spatial artifact during photogrammetry.

2.2. *Spatial artifact*

The design of the spatial artifact was based on the imposed condition that there be as many retroreflective targets visible as possible, at any orientation, and the objective that these visible targets be as far as possible from one another. This artifact is to be used with the C-Track and with the ballbar (using one of the three 0.5″ nests), although it can also be used with the laser tracker (Fig. 4). Indeed, there is no advantage of using such a complex artifact with a laser tracker.

The artifact consists of a steel sphere 45 mm in diameter and with 26 facets. Seven of these facets are used for attaching steel poles 45 mm long, three are used for attaching magnetic nests for 0.5″ spheres (for use with Renishaw's telescopic ballbar), 12 are used for fixing retroreflective self-adhesive targets, and three have threaded holes for future needs (Fig. 4). Six of the steel poles are orthogonal and of slightly different lengths. At the end of each of these six poles, there is a truncated icosahedron (the shape used for soccer balls) with 12 regular pentagonal faces and 20 regular hexagonal faces. Each truncated icosahedron is made by rapid prototyping from black thermoplastic (ABS-700) and has a diameter of about 54 mm. A retroreflective self-adhesive target is fixed on 31 of its 32 facets, randomly offset from the center of each facet. There are a total of 198 retroreflective targets, the retroreflective circle of which is 8 mm in diameter. Finally, the centers of the three magnetic nests are approximately 150 mm away from the robot flange *xy* plane, and 45 mm offset from robot axis 6.

Creaform's MaxSHOT 3D photogrammetry system was used to acquire the position of every target with respect to a common reference frame, located at the centroid of all targets (Fig. 4). The positions of the centers of the three magnetic nests with respect to this reference frame are measured using the HandyPROBE.

This spatial artifact, too, is mounted on an ATI QC-5 tool changer and, along with the three magnetic nests, weighs approximately 2.3 kg. The weight of the complete end-effector is about 2.6 kg. The coordinates of the center of gravity of the complete end-effector are approximately $\{-23$ mm, 0 mm, 100 mm$\}$ with respect to the tool flange reference frame, according to the CAD model of the end-effector. Therefore, both end-effectors exert approximately the same reaction forces and moments on the robot flange.

To the best of our knowledge, very few such spatial artifacts exist. One is the cover of Creaform's MetraSCAN 3D, but this artifact is an integral part of a hand-held 3D scanner and cannot be mounted on the tool flange of a robot. Another is Northern Digital's multisided probe (MSP). The MSP is made of four orthogonal 50 mm struts, with five orthogonally placed active targets at the end of each strut, and weighs only 0.125 kg. The problem with this artifact is that there exist orientations at which no target has a visibility angle of less than 45°. Finally, Booschs *et al.* (2010) presented another spatial

https://doi.org/10.1017/S0263574713000714 Published online by Cambridge University Press

Table I. Pose of the base frame with respect to the world frame with six error parameters.

Parameter	x	y	z	α	β	γ
Value	$x_w + \delta x_w$	$y_w + \delta y_w$	$z_w + \delta z_w$	$\alpha_w + \delta x_w$	$\beta_w + \delta \beta_w$	$\gamma_w + \delta \gamma_w$

*The parameters α, β, and γ are the Euler angles, according to the XYZ convention.

Table II. Complete DHM[23] robot model with 25 error parameters.

i	α_i (°)	a_i (mm)	θ_i (°)	d_i (mm)
1	0	0	θ_1	290
2	$-90 + \delta\alpha_2$	δa_2	$\theta_2 - 90 + \delta\theta_2 + c_2\tau_2$	δd_2
3	$\delta\alpha_3$	$270 + \delta a_3$	$\theta_3 + \delta\theta_3 + c_3\tau_3$	δd_3
4	$-90 + \delta\alpha_4$	$70 + \delta a_4$	$\theta_4 + \delta\theta_4 + c_4\tau_4$	$302 + \delta d_4$
5	$90 + \delta\alpha_5$	δa_5	$\theta_5 + \delta\theta_5 + c_5\tau_5$	δd_5
6	$-90 + \delta\alpha_6$	δa_6	$\theta_6 + 180 + \delta\theta_6 + c_6\tau_6$	$72 + \delta d_6$

artifact made up of 54 active targets equally distributed on a sphere and tracked by a custom optical CMM consisting of four 4-Mpx cameras. The problem with this artifact is that the visible targets are very close to each other.

3. Robot Kinematic Model

The level-3 robot model that we use corresponds to a complete kinematic calibration of the robot, including the base frame, and the five parameters related to the stiffness[11] of joints 2, 3, 4, 5, and 6. Tables I and II show a summary of all 31 parameters.

The location of the nominal robot base frame with respect to the world frame is first measured by rotating joints 1 and 2.[11] The nominal position of the tool frame is also initially measured by rotating joints 5 and 6.[11] However, we will keep the parameters $\delta\theta_6$ and δd_6, which position the tool frame with respect to the robot end-effector frame.

Although neither the laser tracker nor the C-Track are displaced during measurement, the world frame is defined using three 0.5″ magnetic nests fixed in three of the four corners of the robot table (Figs. 2b and 3). All measurements performed with the laser tracker and the C-Track will therefore be taken with respect to a world frame defined by the centers of these three nests. In the first setup, the base is measured only once, using the three 0.5″ SMRs. In the second and third setups, 15 retroreflective self-adhesive targets are attached to the robot base and table.

We define the nominal base frame with respect to frame $\mathcal{F}_1$ (which depends on axes 1 and 2) using the corresponding nominal geometric parameters that relate these axes as follows: the base frame $\mathcal{F}_0$ is obtained by translating $\mathcal{F}_1$, when at the nominal $\theta_1 = 0°$, along the negative direction of its z_1 axis by the nominal offset $d_1 = 290$ mm.

The robot flange frame can be directly measured, by probing the robot flange. However, for various reasons, we chose to identify this frame without having to remove our special-purpose end-effector. In fact, this is often what happens in industry, in the case where a robot is already fully installed and its operators need to calibrate the whole system (i.e., improve the accuracy of the positioning of the tool frame with respect to the world frame) without having to remove the end-effector.

For the nominal $\theta_6 = 0°$, we define $\mathcal{F}_6$ such that its z_6 axis is along axis 6, its x_6 axis is parallel to the normal between axes 5 and 6 and is obtained by normalizing $\mathbf{z}_6 \times \mathbf{z}_5$, and finally, the distance from the normal to x_6 is the nominal distance $d_6 = 72$ mm. The tool frame $\mathcal{F}_{\text{tool}}$ is fixed with respect to F_6, and is therefore measured directly. In the case of the C-Track (setups 2 and 3), the tool frame is the one in which the positions of the retroreflective targets are obtained during photogrammetry. Because the C-Track measures the pose of this frame directly, we chose an end-effector pose that would be visible to the C-Track and reoriented the three SMRs so that all of them would be visible by the laser tracker. In the case of setups 2 and 3, $\mathcal{F}_{\text{tool}}$ is found with respect to $\mathcal{F}_6$. Then, the position of the center of each nest is measured using the HandyPROBE with respect to $\mathcal{F}_{\text{tool}}$ (Fig. 6). In the case of setup 1, we measured the positions of the nests with respect to $\mathcal{F}_6$ directly, as we considered that $\mathcal{F}_{\text{tool}}$ is

https://doi.org/10.1017/S0263574713000714 Published online by Cambridge University Press

Table III. Ranges of motion for each joint for the test, the results of which are shown in Fig. 6.

Joint	Interval	Increment	Tangential error range	Angular error range	Backlash
1	$-60°, 60°$	$5°$	0.114 mm	$0.013°$	$0.004°$
2	$-40°, 40°$	$1°$	1.363 mm	$0.116°$	$0.002°$
3	$-40°, 40°$	$1°$	0.912 mm	$0.098°$	$0.004°$
4	$-155°, 155°$	$5°$	0.445 mm	$0.207°$	$0.037°$
5	$-90°, 90°$	$5°$	0.606 mm	$0.153°$	$0.017°$
6	$-400°, 400°$	$1°$	0.156 mm	$0.072°$	$0.037°$

coincident with $\mathcal{F}_6$. Note that in all three setups, the positioning accuracy of the robot is evaluated at the centers of the magnetic nests, and so the location of $\mathcal{F}_{\text{tool}}$ has no effect on the final results.

4. Analysis of Nonkinematic Robot Behavior

It is often said that the nongeometric errors in an industrial robot (such as joint compliance) affect the robot accuracy very little, but this is not true for robots such as the ABB IRB 120, which use harmonic drive gearboxes. To gain an insight into the elastic behavior of the robot, a series of simple tests was performed.

4.1. Axis analysis with the laser tracker

A third end-effector was used for these tests. The weight of this end-effector is 2.75 kg and its center of gravity is located at $\{-31$ mm, -13 mm, 85 mm$\}$ with respect to $\mathcal{F}_6$. One $1.5''$ SMR is attached at position $\{-114.4$ mm, -46.2 mm, 124.5 mm$\}$ with respect to $\mathcal{F}_6$. The position of this SMR is measured with the laser tracker when each joint is displaced in equal increments within an interval (Table III), first in the positive and then in the negative direction, while the other five joints are kept at $0°$. (The configuration with all joints at $0°$ is shown in Fig. 5). For each joint, errors are calculated with respect to the circle centered at the joint axis (obtained by least squares using all the measurements of each axis) and passing through the position of the target when the joint is at $0°$. Radial and axial displacements are in the order of 0.050 mm, mostly corresponding to measurement noise. Therefore, we only analyze the tangential error, caused mainly by the elasticity of the gearboxes (Fig. 5).

Note that the backlash between positive and negative rotation is very small for joints 1, 2, and 3 (less than $0.005°$), which is because of the harmonic drives. However, it is relatively large for joints 4, 5, and 6, which also use harmonic drives.

The tangential errors shown in Fig. 5 are clearly due to the elasticity of the gear boxes. The displacement of joint 1 and joint 6 contributes to the smallest errors. In fact, there is virtually no change in the deflection of the robot as measured at the end-effector, since axis 1 is parallel to the direction of gravity. Note that only the range $[-200°, 200°]$ is displayed for axis 6, since the errors are no larger for the full range. This is because the motor and the harmonic drive gearbox of joint 6 are directly installed in link 6.

Due to the varying gravity effect of the robot arm as a function of θ_2 and the long lever effect, the tangential errors caused by rotating joints 2, 3, and 5 are significant, and should be taken into account in the stiffness model. The tangential error associated with joints 4 and 6 is smaller, but will also be taken into account. In fact, note that the peaks for these two joints are separated by $180°$. This deflection is due mainly to the weight of the SMR and to an extra load mounted beneath SMR. In other words, if the center of gravity of the end-effector were farther from axis 6, the errors would have been much larger.

4.2. Stiffness model

As previously mentioned, a five-parameter model is used to represent the elastic behavior of the robot.[11] This model takes into account the elasticity of the gearboxes of joints 2, 3, 4, 5, and 6 (one parameter per joint). The elasticity in each gearbox is modeled as a linear torsional spring, so this parameter represents the effective constant compliance c_i of each joint i. Traction and compression effects are neglected. Torsional effects are also neglected.

https://doi.org/10.1017/S0263574713000714 Published online by Cambridge University Press

Table IV. Masses and centers of gravity of each robot link in our model.

i	m_i (kg)	$c^i_{x,i}$ (mm)	$c^i_{y,i}$ (mm)	$c^i_{z,i}$ (mm)
1	0	0	0	0
2	4.2	140	0	0
3	0	0	0	0
4	5	0	0	−193.6
5	0	0	0	0
6 (Triangular artifact)	2.6	−23	0	100
6 (Spatial artifact)	2.7	50	25	100

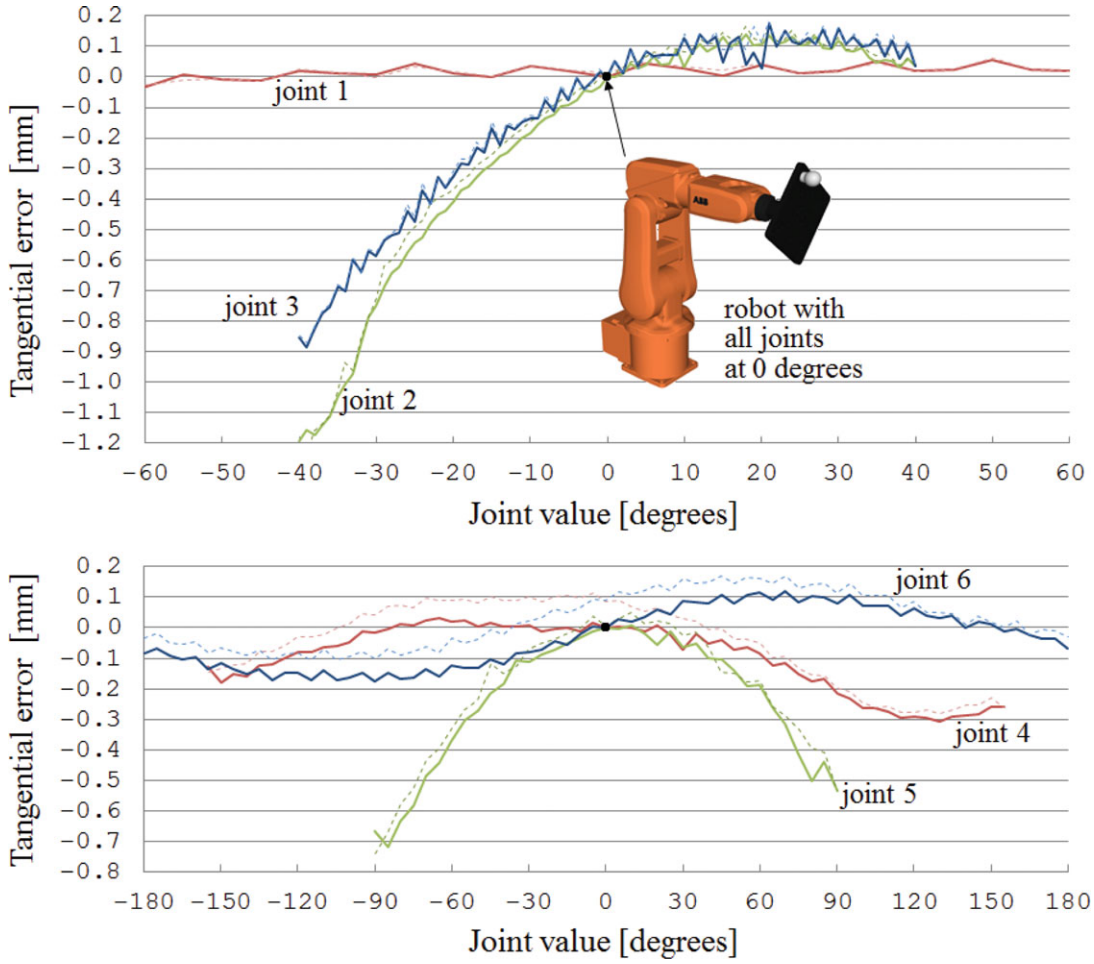

Fig. 5. (Colour online) Tangential errors measured when rotating a single joint.

We took into account the gravity forces due to the masses of links 2, 3, and 4 and the tool. We neglected the masses of links 5 and 6, as they are relatively small, as well as the mass of link 0 (the base). The mass of link 1 is not needed, because we did not consider a compliance parameter to model the flexibility of joint 1, since the axis of that joint is parallel to the gravity vector. We simplified the specifications provided by ABB into the parameters shown in Table IV.

Note that links 3 and 4 are considered as one, and the effect of link 3 is transferred to link 4. The center of gravity of these two links lies on axis 4, and therefore the compliance parameter for that axis is not affected by the weight of links 3 and 4.

https://doi.org/10.1017/S0263574713000714 Published online by Cambridge University Press

5. Calibration

The complete model consists of 31 error parameters: 6 parameters to locate the robot base frame, 20 geometric parameters (4 D-H M parameters for links 2 to 6), and 5 compliance parameters (for joints 2–6). However, since axes 2 and 3 are parallel, and because we find the parameters by linearization of the system, one of the 20 geometric parameters becomes redundant and so we exclude it from the model.

In order to minimize the backlash effect, the robot is first moved, in absolute joint mode (*MoveAbsJ*), to the configuration $\{\theta_1 - 5^\circ, \theta_2 - 5^\circ, \theta_3 - 5^\circ, \theta_4 - 5^\circ, \theta_5 - 5^\circ, \theta_6 - 5^\circ\}$ and then to the final configuration $\{\theta_1, \theta_2, \theta_3, \theta_4, \theta_5, \theta_6\}$ for each calibration or validation robot configuration. Furthermore, $\theta_2 \geq 0^\circ$ and $\theta_3 \geq -80^\circ$, in order to keep the torques in joints 2 and 3 negative and be able to use a linear model for the stiffness of the gearboxes, which are, in fact, much less stiff when they are not loaded. In addition, the workspace of the robot is further limited by imposing $-90^\circ \geq \theta_1 \geq 90^\circ$, in order to maximize the visibility of both artifacts, and $-150^\circ \geq \theta_4 \geq 150^\circ$, $-90^\circ \geq \theta_5 \geq 90^\circ$, and $-180^\circ \geq \theta_6 \geq 180^\circ$ because of the tool changer pneumatic hoses. Finally, we recall that in each of the three setups, the range of end-effector orientations is quite different, being virtually unlimited in the third setup.

5.1. System linearization

All the kinematic error parameters are considered very small. Those of the base are $[\delta x_b, \delta y_b, \delta z_b, \delta\alpha_b, \delta\beta_b, \delta\gamma_b]$ according to Table I, those of link 2 are $[\delta\alpha_2, \delta a_2, \delta\theta_2, \delta d_2]$ according to the third row of Table II, etc. The robot model can be expressed as

$$\mathbf{f} = \mathbf{f}(\mathbf{p}, \mathbf{q}), \tag{1}$$

where $\mathbf{f} = [x, y, z]^T$ is the position of the end-effector (note that only the position data are taken into account), $\mathbf{p}$ is the vector containing all 31 error parameters, and $\mathbf{q} = [\theta_1, \theta_2, \ldots, \theta_6]^T$ is the vector of the joint variables. The expression of Eq. (1) is quite complex, because it is a function of 37 parameters and other constant parameters, like masses and centers of gravity. If we derive the Jacobian matrix of this robot model, the expression becomes even more complex. Fortunately, this expression can be obtained easily using the MATLAB Symbolic Toolbox, so the linearized equations can be expressed at iteration i as

$$\Delta\mathbf{f}^i = \mathbf{J}^i \Delta\mathbf{p}^i, \tag{2}$$

where $\Delta\mathbf{f}^i$ is the difference between the measured position and the position predicted by the model for a given robot configuration, $\mathbf{J}^i$ is the Jacobian matrix, and $\Delta\mathbf{p}^i$ are the values to add to the error parameters. Using enough end-effector position measurements for different robot configurations, we can obtain the least squares solution of the error parameters using the pseudoinverse of the Jacobian:

$$\Delta\mathbf{p} = (\mathbf{J}^{\mathrm{T}}\mathbf{J})^{-1}\mathbf{J}^{\mathrm{T}}\Delta\mathbf{f}. \tag{3}$$

The Jacobian is slightly different at each iteration, because it depends on the error parameters found in each step, where we verify that all the columns of $\mathbf{J}$ are linearly independent. If they are not, we must discard the useless error parameters. When we verified the linear independency in our case, the error parameters δd_2 and δd_3were found to be linearly dependent (because of the parallel axes), and so ultimately, we did not consider δd_3 in the model. We also realized that the solution was stable after four iterations.

5.2. Observability

To measure the goodness of a set of robot configurations, we used an observability index and an iterative algorithm.[11,24] This index emphasizes the volume of a hyperellipsoid,[16] the directions of which are represented by the singular values:[7]

$$O = \frac{\sqrt[m]{\sigma_1\sigma_2\ldots\sigma_m}}{\sqrt{n}}, \tag{4}$$

https://doi.org/10.1017/S0263574713000714 Published online by Cambridge University Press

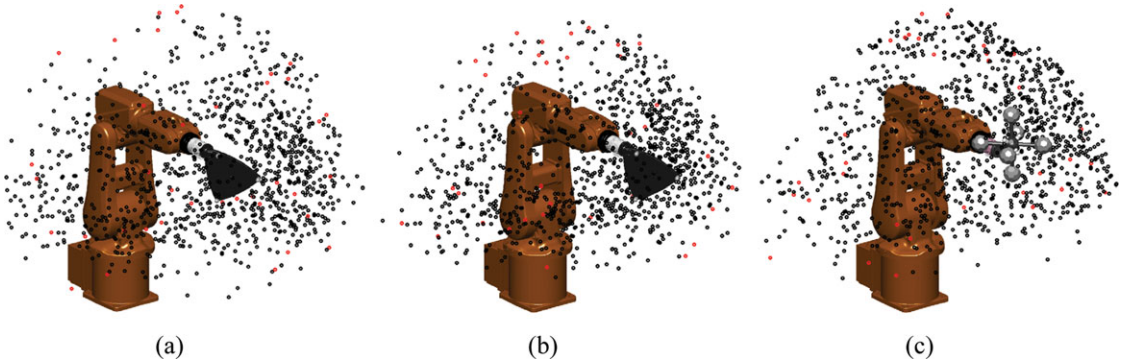

Fig. 6. (Colour online) Calibration and validation positions using (a) the laser tracker and the triangular artifact (setup 1); (b) the C-Track and the triangular artifact (setup 2); (c) the C-Track and the spatial artifact (setup 3).

where n is the number of configurations, m is the number of error parameters, and σ_i are the singular values of the singular value decomposition:

$$\mathbf{J} = \mathbf{U}\Sigma\mathbf{V}', \tag{5}$$

where

$$\Sigma = \begin{bmatrix} \sigma_1 & 0 & \cdots & 0 \\ \vdots & \vdots & \vdots & \vdots \\ 0 & 0 & \cdots & \sigma_m \\ 0 & 0 & \cdots & 0 \\ \vdots & \vdots & \vdots & \vdots \\ 0 & 0 & \cdots & 0 \end{bmatrix}. \tag{6}$$

We applied a numerical algorithm to find a good set of calibration measurements for each of the three setups.[11] With a random set of 5000 robot configurations and a random start subset of 11 of them, we use an iterative algorithm to change this subset to obtain a better observability index. At each iteration, we remove from the subset the configuration that leaves the highest observability index (if the index increases by removing a configuration) and we add the configuration that results in the highest observability index (again, if adding a configuration increases the observability index). Finding the optimal subset of calibration configurations is performed offline, through simulations.

5.3. Laser tracker and triangular artifact (setup 1)

The base reference frame is measured only once, using the three nests placed on the table depicted in Figs. 2(b) and 3. For each robot configuration, we measure the position of only one of the three SMRs (as shown in Fig. 2b). Figure 6(a) shows the positions of the SMR that is measured, with those corresponding to calibration configurations depicted in red. There are only 38 calibration configurations, which are found using the observability study previously explained. The remaining black dots correspond to the position of one of the three SMRs in the 1000 random robot configurations used for validating the efficiency of the robot calibration.

5.4. C-Track and triangular artifact (setup 2)

As already mentioned, both the front face and the back face of the triangular artifact are measured in the second setup. However, the back side is visible in only one of every five robot configurations. For each configuration, we measure the pose of the triangular artifact $\mathcal{F}_{\text{tool}}$ with respect to the base $\mathcal{F}_{\text{world}}$. The positions of the origin of $\mathcal{F}_{\text{tool}}$ (Fig. 7a) corresponding to each robot configuration measurement are shown in Fig. 6(b). We found 36 calibration configurations, depicted in red, using the observability study explained above. The black dots correspond to the 1000 random robot configurations used to validate the calibrated model. In this study, we did not consider a measurement to be valid unless there were a minimum of 12 and 9 visible targets from the base and end-effector, respectively.

https://doi.org/10.1017/S0263574713000714 Published online by Cambridge University Press

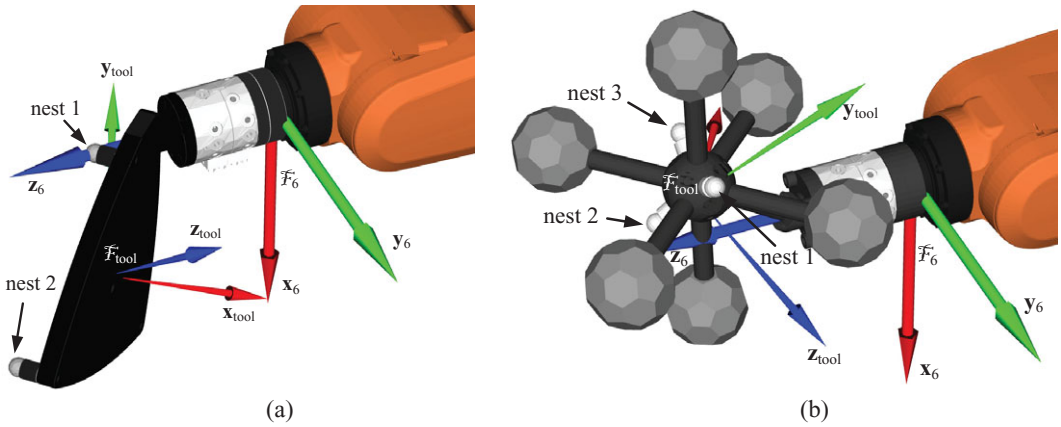

Fig. 7. (Colour online) The positions of the three magnetic nests with respect to $\mathcal{F}_6$ are measured directly.

Note that although the C-Track measures the pose of the robot end-effector, we only consider the position of all three magnetic nests (on the robot end-effector). Consequently, for each robot configuration measured, we have the position of all three magnetic nests.

5.5. C-Track and spatial artifact (setup 3)

As in setup 2, we measure the pose of the spatial artifact $\mathcal{F}_{\text{tool}}$ with respect to the base frame $\mathcal{F}_{\text{world}}$ in each robot configuration. The positions of the origin of $\mathcal{F}_{\text{tool}}$ (Fig. 7b) corresponding to each robot configuration measurement are shown in Fig. 6(c). There are 35 calibration configurations, in red, which are found using the observability study explained. The black dots correspond to the 1000 random robot configurations used to validate the calibrated model. In this study, we did not consider a measurement to be valid unless there were a minimum of 12 and 20 visible targets from the base and end-effector, respectively.

6. Results

The calibration method was first tested with simulations using the robot model described in Section 3. Forcing a set of error parameters that provoke a nominal position measurement of 5 mm (maximum value), the maximum position measurement error after calibration is 0.004 mm, if we do not consider noise measurement and if the masses and their centers of gravity are perfectly known (note that these parameters are not identified by the model). If we apply a measurement noise of 0.070 mm and consider a 10% error for the masses and centers of gravity, the mean/maximum position measurement errors are in the order of 0.050–0.100 mm for the 1000 random robot configurations for each of the three setups. We also tried several other observability indices[17–19] (with simulation and experimental results), but the results we obtained were worse.

Note, too, that the 0.004 mm error after calibration and without noise measurement is due to the parametric redundancy caused by the consecutive and parallel axes 2 and 3. This error is so small that we discarded a specific link model between these two joints to properly represent the physical link (such as the CPC model[3,20–22]).

Finally, to perform the experimental tests, the robot was warmed up for 1 h and then programmed to go to the planned configurations with the end-effector speed limited to 500 mm/s and 20°/s. Furthermore, for each robot configuration, the robot was programmed to pause for 4 s while either the laser tracker or the C-Track performed the measurement. As already mentioned, the measurement acquisition process is fully automated.

6.1. Analysis of the measurement devices

To evaluate the volumetric accuracy of each of the two measurement systems, both artifacts were measured on a Mitutoyo Bright-STRATO 7106 CMM with a total measurement uncertainty of 0.0027 mm at a 95% confidence level. The setup is shown in Fig. 8. Four 0.5″ precision balls were

https://doi.org/10.1017/S0263574713000714 Published online by Cambridge University Press

Table V. Distance errors for the C-Track and the laser tracker with respect to the CMM.

	Nest 1 (on the artifact)	Nest 2 (on the artifact)	Nest 3 (on the artifact)	Nest 4 (on the base)	
Triangular artifact	Laser tracker	0.034 mm	0.029 mm	0.035 mm	0.034 mm
	C-Track	0.124 mm	0.061 mm	0.082 mm	0.124 mm
Spatial artifact	Laser tracker	0.015 mm	0.015 mm	0.010 mm	0.038 mm
	C-Track	0.129 mm	0.118 mm	0.138 mm	0.177 mm

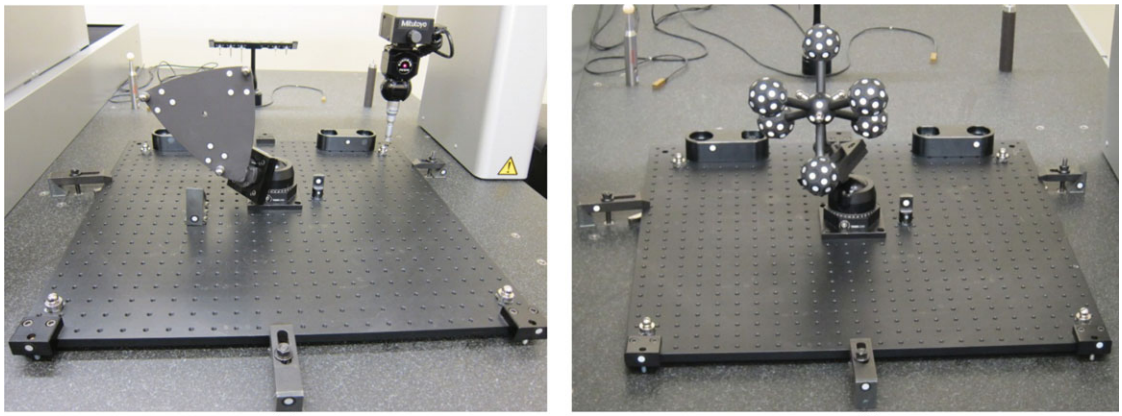

(a) (b)

Fig. 8. (Colour online) Accuracy validation of the C-Track and laser tracker on the CMM.

mounted on magnetic nests that were fixed with respect to the granite base of the CMM. Three of these balls were used to define the common reference frame, and, for each artifact, the coordinates of the centers of the three magnetic nests were measured with respect to that frame. In each setup, all seven centers were first measured by the CMM (by probing 0.5″ precision balls), then by the laser tracker (using 0.5″ SMRs), and finally by the C-Track (measurements obtained indirectly from the pose of the artifact).

In the case of the C-Track, the pose of the end-effector was measured with respect to a set of eight retroreflective targets fixed with respect to the CMM's granite table. The centers of the four magnetic nests mounted on the base were measured using the HandyPROBE (equipped with a 0.5″ precision ball tip) with respect to the eight targets. In a previous step, the positions of the centers of the magnetic nests on each artifact with respect to the photogrammetry frame were measured using the HandyPROBE.

Table V shows the distance errors between the centers of four of the seven magnetic nests measured using the C-Track and the laser tracker with respect to the centers measured by the CMM. All the measurements were taken by the CMM, the C-Track, and the laser tracker with respect to the common reference frame defined by three of the four magnetic nests mounted on the base of the CMM. The first three nests in Table V are the ones mounted on the artifact, while the fourth is the one mounted on the base and not used to define the common reference frame (the one being probed in Fig. 8a).

We performed the same test for two other orientations for each artifact, and the results were very similar to the ones presented in Table V. Nevertheless, these tests are inconclusive, and do not necessarily give an estimate of the volumetric accuracy of either the laser tracker or the C-Track. However, they demonstrate that in perfect laboratory conditions, the accuracy of the C-Track is worse than that of the laser tracker, especially in the case of the spatial artifact.

6.2. Validation using the laser tracker and the C-Track

The validation tests compare the position errors at the three magnetic nests on each of the end-effectors with respect to the world reference frame defined on the robot table, between the uncalibrated robot and the calibrated one, in 1000 random robot configurations (which are different for the three setups).

https://doi.org/10.1017/S0263574713000714 Published online by Cambridge University Press

Table VI. Robot base errors obtained with the laser tracker and the triangular artifact.

Parameter	δx_w (mm)	δy_w (mm)	δz_w (mm)	$\delta \alpha_w$ (°)	$\delta \beta_w$ (°)	$\delta \gamma_w$ (°)
Value	−0.075	−0.096	0.103	0.003	0.008	−0.033

Table VII. Robot model obtained with the laser tracker and the triangular artifact.

i	α_i (°)	a_i (mm)	θ_i (°)	d_i (mm)
1	0.000	0.000	θ_1	290.000
2	−90.006	0.134	$\theta_2 - 89.909 + 0.032 \times 10^{-6}\ \tau_2$	0.000
3	−0.011	270.236	$\theta_3 + 0.054 + 0.130 \times 10^{-6}\ \tau_3$	0.006
4	−90.009	70.138	$\theta_4 - 0.027 + 0.605 \times 10^{-6}\ \tau_4$	302.246
5	89.984	−0.061	$\theta_5 + 0.067 + 0.419 \times 10^{-6}\ \tau_5$	−0.067
6	−89.969	0.022	$\theta_6 + 179.913 + 0.647 \times 10^{-6}\ \tau_6$	72.050

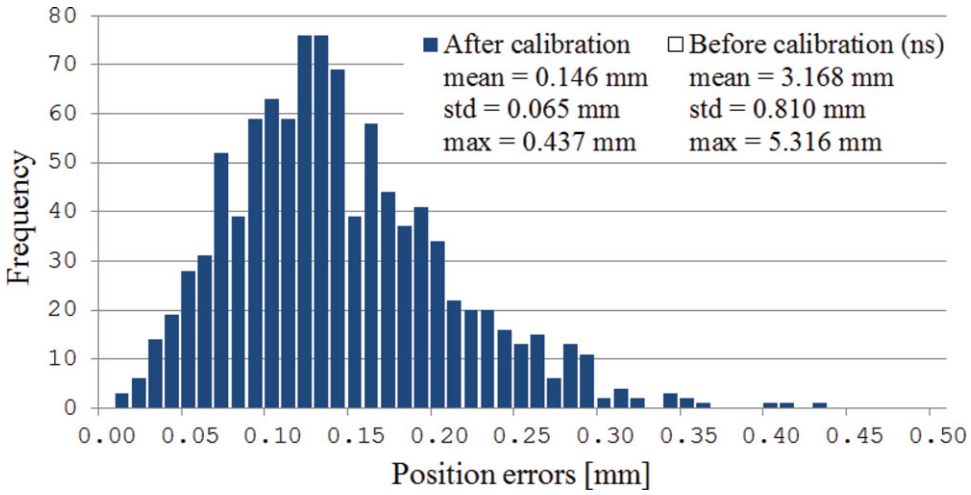

Fig. 9. (Colour online) Histogram of position errors using the laser tracker and the triangular artifact.

For each setup, the results are shown in the form of a histogram of the position errors, and a list of the parameters identified is included.

It is very surprising that the nominal position accuracy of the ABB IRB 120 robot is worse than 5 mm. Note that the nominal model used is the one that corresponds to the nominal geometric parameters of the robot, but includes the base and tool frame identifications previously described. In other words, if these frames had been measured by probing the robot base and robot tool flange instead, the accuracy of the nominal model would most probably have been worse.

6.2.1. Laser tracker with triangular artifact (setup 1). Figure 9 shows the accuracy results after calibration for the 1000 position measurements illustrated in Fig. 6(a). For clarity, the results before calibration are not shown. Suffice to say that the mean position error improved from 3.168 to 0.146 mm. The robot model obtained after calibration is shown in Tables VI and VII. As can be seen, the errors are very small, but their combined effect is large.

6.2.2. C-Track with triangular artifact (setup 2). Figure 10 shows the position errors after calibration for 3000 measurements of the centers of the three magnetic nests, obtained using the pose measurement of the 1000 configurations illustrated in Fig. 6(b). The errors before calibration are not shown, since they are too large. The mean position error improved from 4.639 to 0.176 mm. The robot model obtained after calibration is shown in Tables VIII and IX. Clearly, the robot accuracy after calibration is very similar to that obtained when calibrating with a laser tracker.

Note that the nominal accuracy for this test is much worse than for the previous test. This may be because we had to modify the position of the end-effector orientation when moving axes 1 and 2

https://doi.org/10.1017/S0263574713000714 Published online by Cambridge University Press

Table VIII. Robot base errors obtained with the C-Track and the triangular artifact.

Parameter	δx_w (mm)	δy_w (mm)	δz_w (mm)	$\delta \alpha_w$ (°)	$\delta \beta_w$ (°)	$\delta \gamma_w$ (°)
Value	0.047	2.403	−0.994	0.118	0.028	−0.070

Table IX. Robot model obtained with the C-Track and the triangular artifact.

i	α_i (°)	a_i (mm)	θ_i (°)	d_i (mm)
1	0.000	0.000	θ_1	290.00
2	−90.008	0.052	θ_2−89.891+ 0.028× 10^{-6} τ_2	0.048
3	−0.023	270.223	θ_3+0.071+ 0.122× 10^{-6} τ_3	0.000
4	−90.015	70.164	θ_4−0.027+ 0.646× 10^{-6} τ_4	302.187
5	89.988	−0.086	θ_5+0.062+ 0.476× 10^{-6} τ_5	0.009
6	−89.982	−0.007	θ_6+180.000+ 0.243× 10^{-6} τ_6	72.373

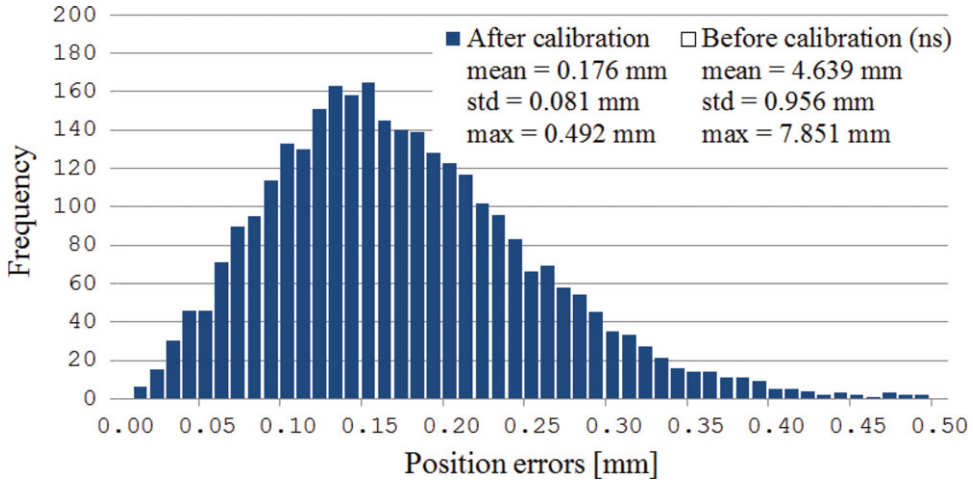

Fig. 10. (Colour online) Histogram of position errors using the C-Track and the triangular artifact.

to identify the base frame so that the front side of the tool was facing the C-Track within a ± 30° range. We can clearly see that after calibration, the errors made when measuring the base frame were quite significant ($\delta y_w = 2.403$ mm and $\delta y_w = -0.994$ mm). These errors in the base only affect the nominal model, however, and are probably due to the flexibility behavior of the robot, which seems to be quite different when the wrist angles are changed (while moving axes 1 and 2, we kept $\theta_3 = \theta_4 = 0°$, $\theta_5 = -40°$, and $\theta_6 = 80°$). The results for the robot parameters are very similar (Table IX vs. Table VII).

6.2.3. C-Track with spatial artifact (setup 3). Figure 11 shows the accuracy results after calibration for the 3000 position measurements of the centers of the three magnetic nests, obtained using the pose measurement of the 1000 configurations illustrated in Fig. 6(c). The mean position error improved from 2.913 to 0.149 mm. The robot model obtained after calibration is shown in Tables X and XI. The robot accuracy after calibration in this setup is very similar to the accuracy obtained in the first two setups.

6.3. Validation using a telescopic ballbar

The results shown in Figs. 9–11 suggest that the C-Track is as effective as the laser tracker in calibrating the ABB IRB 120 robot. However, these validation results are not directly comparable, since the robot configurations (although random and excessive in number) are not the same and are not measured with the same tool. Therefore, in order to perform a fair comparison, the efficiency of the three robot calibrations was tested using a QC20-W telescopic ballbar by Renishaw in the same (for calibration models 1 and 2) and almost the same (for calibration model 3) set of robot configurations

https://doi.org/10.1017/S0263574713000714 Published online by Cambridge University Press

Table X. Robot base errors obtained with the C-Track and spatial artifact.

Parameter	δx_w (mm)	δy_w (mm)	δz_w (mm)	$\delta \alpha_w$ (°)	$\delta \beta_w$ (°)	$\delta \gamma_w$(°)
Value	−0.099	0.024	0.184	0.003	−0.012	−0.023

Table XI. Robot model obtained with the C-Track and the spatial artifact.

i	α_i (°)	a_i (mm)	θ_i (°)	d_i (mm)
1	0.000	0.000	θ_1	290.000
2	−90.013	0.095	θ_2−89.914+ 0.037× 10^{-6} τ_2	−0.024
3	−0.018	270.156	θ_3+0.073+ 0.112× 10^{-6} τ_3	0.000
4	−90.018	70.153	θ_4−0.026+ 0.462× 10^{-6} τ_4	302.232
5	89.995	−0.055	θ_5+0.064+ 0.301× 10^{-6} τ_5	0.062
6	−90.004	0.004	θ_6+179.946+2.000× 10^{-6} τ_6	71.991

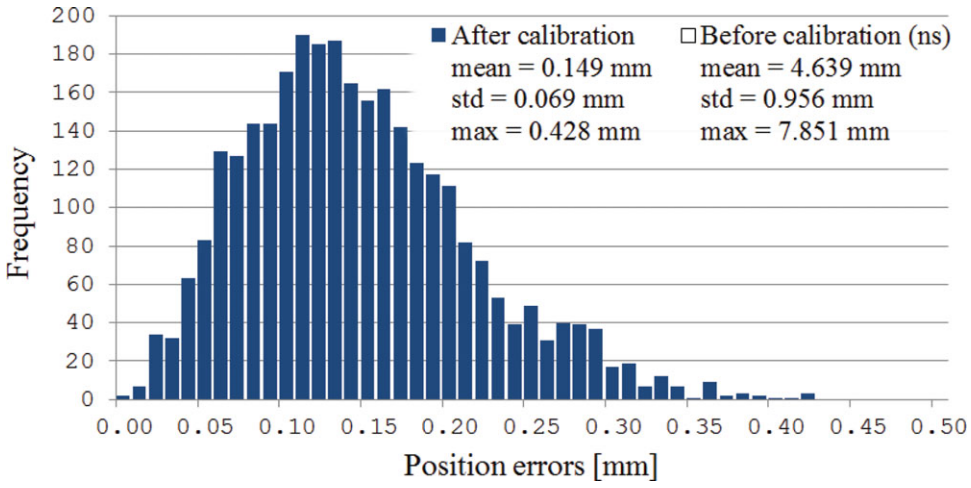

Fig. 11. (Colour online) Histogram of position errors using the C-Track and the spatial artifact.

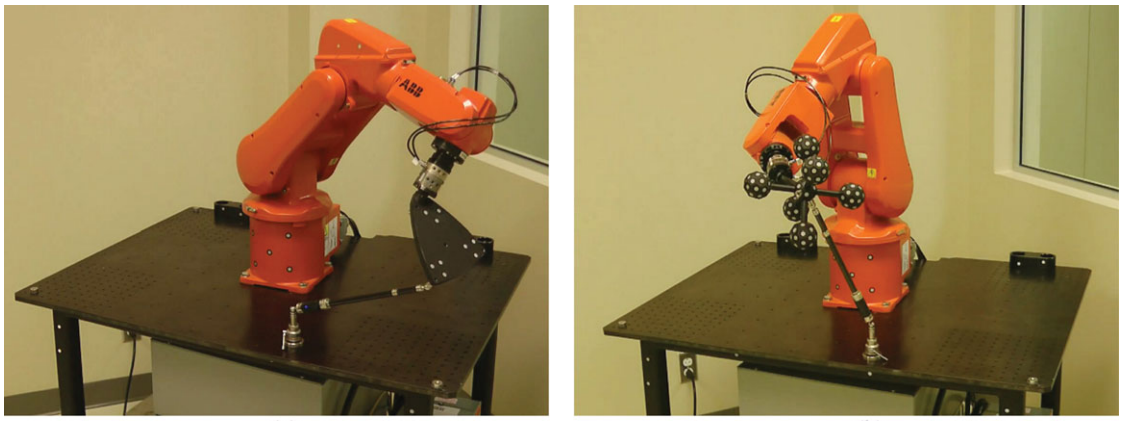

Fig. 12. (Colour online) Measuring distance accuracy with a Renishaw telescopic ballbar.

and in the same manner (Fig. 12). The ballbar sensor accuracy (at 20°C) is ±0.5 μm, and its measuring range is only ±1.0 mm, which is why we have no measurements for the nominal model.

The three calibration models were used to perform the spherical ballbar tests, around the same center point at a radius of 300 mm, and at a speed limited to 500 mm/s and 20 degrees/s. The robot pauses for 2 s before each measurement (we repeated the tests twice, and found that the results

https://doi.org/10.1017/S0263574713000714 Published online by Cambridge University Press

Table XII. Summary of ballbar results obtained using the triangular artifact.

Ballbar attached to	Robot model	Mean error	Standard deviation	Maximum error
Nest 1	Laser tracker	−0.105 mm	0.091 mm	0.327 mm
	C-Track	0.022 mm	0.110 mm	0.250 mm
Nest 2	Laser tracker	−0.148 mm	0.118 mm	0.437 mm
	C-Track	−0.048 mm	0.135 mm	0.363 mm

Table XIII. Summary of ballbar results obtained using the spatial artifact.

Ballbar attached to	Robot model	Mean error	Standard deviation	Maximum error
Nest 1	C-Track	0.091 mm	0.126 mm	0.328 mm
Nest 3	C-Track	0.146 mm	0.130 mm	0.385 mm

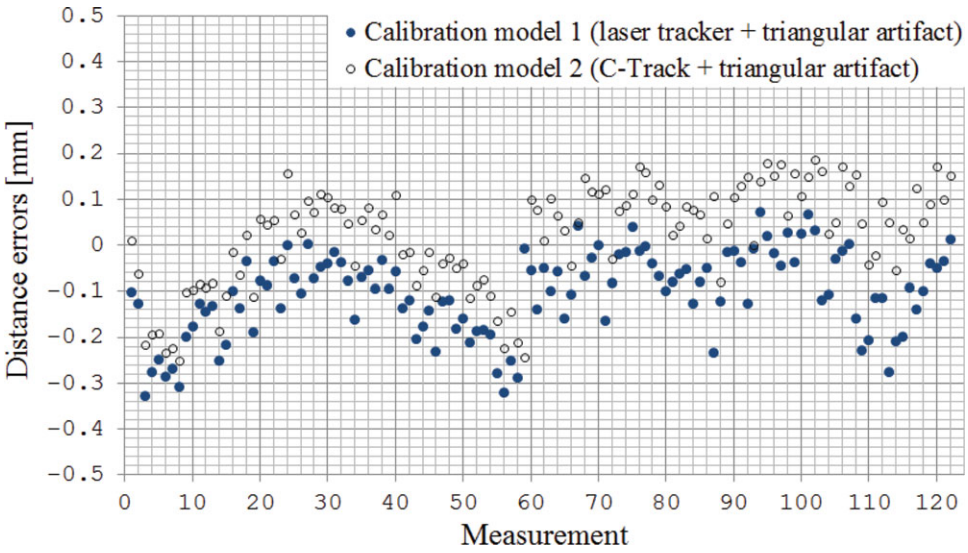

Fig. 13. (Colour online) Results for the path with the ballbar attached to nest 1 of the triangular artifact.

were very repeatable). The ballbar is magnetically attached to two nests of the end-effector (using a different path for each nest). The center of the sphere was taught to the robot manually, using nest 1 for both artifacts. Finally, note that we do not perform the backlash suppression procedure that we use when measuring with the laser tracker or the C-Track.

6.3.1. Results using the triangular artifact. Figures 13 and 14 show the results of the two paths performed with the triangular artifact, with the ballbar attached to nests 1 and 2, respectively. The laser tracker model (calibration model 1) and the C-Track model (calibration model 2) are therefore directly compared. The first path consists of 123 ballbar measurements using nest 1 (Fig. 13), and the second path consists of 95 ballbar measurements using nest 2 (Fig. 14).

From Figs. 13 and 14, we can see that the two calibrations result in similar improvements for each robot configuration. From Table XII, however, we can see that the overall efficiency of the robot calibration with the C-Track is better.

6.3.2. Results using the spatial artifact. Figures 15 and 16 show the results of the two paths performed with the spatial artifact, with the ballbar attached to nests 1 and 3, respectively. Only calibration model 3 (C-Track and spatial artifact) is shown. The first path consists of 108 ballbar measurements using nest 1, and the second path consists of 90 ballbar measurements using nest 3. The center of the sphere is the same as the one used for the paths of the triangular artifact (Fig. 12).

These results are similar to the results obtained using the triangular artifact (Table XIII). Note, however, that the robot configurations are not exactly the same and neither are the measurements points.

https://doi.org/10.1017/S0263574713000714 Published online by Cambridge University Press

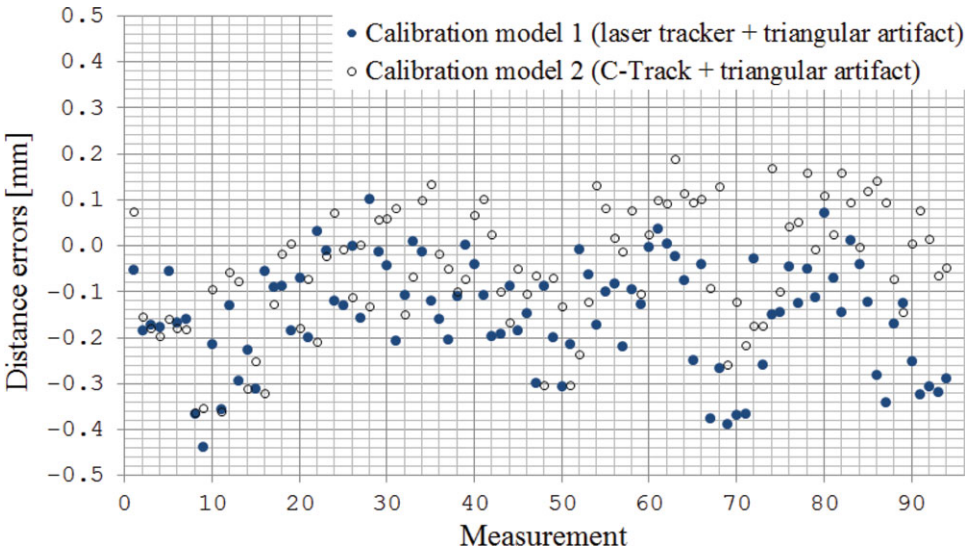

Fig. 14. (Colour online) Results for the path with the ballbar attached to nest 2 of the triangular artifact.

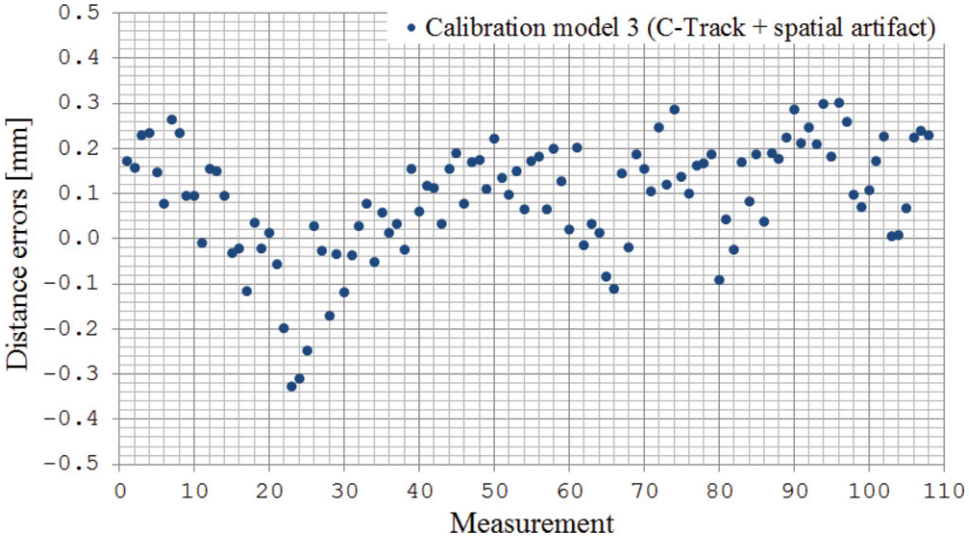

Fig. 15. (Colour online) Results for the path with the ballbar attached to nest 1 of the spatial artifact.

7. Conclusions

We demonstrated clearly that the efficiency of the C-Track in calibrating the ABB IRB 120 industrial robot is equivalent to that of the FARO laser tracker, and costs half as much. We also demonstrated, to our surprise, that there is no benefit to using the C-Track with a complex spatial artifact that allows the pose of the robot end-effector to be measured in any orientation. It is very difficult to manufacture such an artifact, to inspect it through photogrammetry, or even to handle it, so this observation comes as a relief.

The C-Track has another advantage over the laser tracker. To acquire the laser tracker measurements, we need to make an initial guess as to the location of the target. Otherwise, the laser tracker will spend too much time searching for the SMR. Of course, we could track dynamically and always measure the same SMR, but measuring three SMRs (as we do) gives much better results that measuring only one.

Furthermore, we showed that a relatively simple calibration model with only five nongeometric error parameters can improve the volumetric accuracy of the ABB IRB 120 industrial robot significantly. In fact, the mean and maximum position errors were reduced from more than 3 and 5 mm, respectively, to about 0.150 and 0.500 mm. Note that if we do not use the five compliance

https://doi.org/10.1017/S0263574713000714 Published online by Cambridge University Press

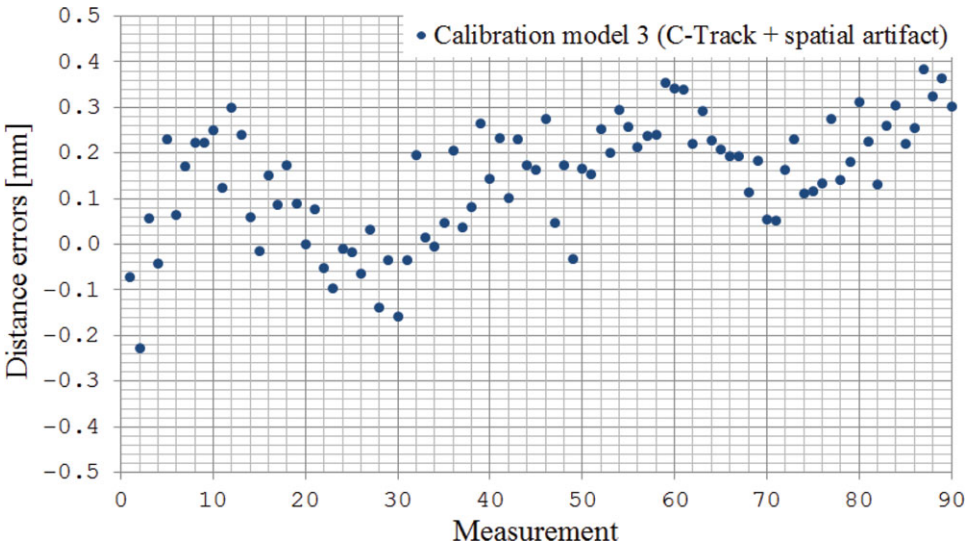

Fig. 16. (Colour online) Results for the path with the ballbar attached to nest 3 of the spatial artifact.

parameters in our robot model, the mean and maximum position errors are reduced to only 0.4 and 1.0 mm approximately.

Our calibration procedure, especially in the case of the C-Track, is very quick. In order to calibrate the robot using the C-Track and the triangular artifact, we need only measure the pose of the robot end-effector in 36 robot configurations. In contrast, ABB uses 100 position measurements taken with a Leica laser tracker.

In conclusion, we demonstrated for the first time that using Creaform's C-Track and a simple planar end-effector to calibrate a small industrial robot is as efficient as when using a laser tracker, yet much cheaper, quicker, and easier.

Acknowledgements

We thank the Canada Research Chair program and the Natural Sciences and Engineering Research Council of Canada for financing this work. We also express our gratitude to Dr. Torgny Brogardh, Corporate Executive Engineer at ABB Robotics, for his help in preparing the work. We also thank "La Caixa" d'estalvis i pensions de Barcelona. Finally, we thank Creaform for lending us a C-Track, performing the photogrammetry of our artifacts, and assisting us with some of the tests.

References

1. Z. Roth, B. Mooring and B. Ravani, "An overview of robot calibration," *IEEE J. Robot. Autom.* **3**(5), 377–385 (1987).
2. S. Besnard, W. Khalil and G. Garcia, "Geometric Calibration of Robotics Using Multiple Plane Constraints," **In**: *Advances in Robotic Kinematics* (Kluwer Academic Publishers, Norwell, MA, 2000) pp. 61–70.
3. S. Hayati and M. Mirmirani, "Improving the absolute positioning accuracy of robot manipulators,"*J. Robot. Syst.* **2**(4), 397–413 (1985).
4. M. Driels, "Using passive end-point motion constraints to calibrate robot manipulators," *J. Dyn. Syst. Meas. Control* **115**(3), 560–566 (1993).
5. N. Juneja and A. Goldenberg, "Kinematic Calibration of a Re-Configurable Robot (RoboTwin)," *Proceedings of the 1997 IEEE International Conference on Robotics and Automation (ICRA)*, Albuquerque, NM, USA (1997) pp. 3178–3183.
6. L. Beyer and J. Wulfsberg, "Practical robot calibration with ROSY," *Robotica* **22**(5), 505–512 (2004).
7. H. Stone and A. Sanderson, "A Prototype Arm Signature Identification System," *Proceedings of the IEEE International Conference on Robotics and Automation*, Raleigh, NC, USA (1987) pp. 175–182.
8. G. Puskorius and L. Feldkamp,"Global Calibration of a Robot/Vision System," *Proceedings of the 1987 IEEE International Conference on Robotics and Automation*, Raleigh, NC, USA (1987) pp. 190–195.
9. Y. Meng and H. Zhuang,"Self-calibration of camera-equipped robot manipulators," *Int. J. Robot. Res.* **20**(11), 909–921 (2001).

https://doi.org/10.1017/S0263574713000714 Published online by Cambridge University Press

10. C. Dumas, S. Caro, M. Chérif, S. Garnier and B. Furet,"A Methodology for Joint Stiffness Identification of Serial Robots," *Proceedings of the 2010 IEEE International Conference on Intelligent Robots and Systems* (2010) pp. 464–469.
11. A. Nubiola and I. A. Bonev, "Absolute calibration of an ABB IRB 1600 robot using a laser tracker," *Robot. Comput.-Integr. Manuf.* **29** (1), 236–245 (2013).
12. B. W. Mooring and S. S. Padavala, "The Effect of Kinematic Model Complexity on Manipulator Accuracy," *Proceedings of the 1989 IEEE International Conference on Robotics and Automation*, Scottsdale, AZ, USA (1989) pp. 593–598.
13. C. Lightcap, S. Hamner, T. Schmitz and S. Banks, "Improved positioning accuracy of the PA10–6CE robot with geometric and flexibility calibration," *IEEE Trans. Robot.* **24**(2), 452–456 (2008).
14. F. Booschs, R. Schütze, C. Simon, F. Zarzani, H. Wirth and J. Meier, "Increasing the Accuracy of Untaught Robot Positions by Means of a Multi-Camera System," *Proceedings of 2010 International Conference on Indoor Positioning and Indoor Navigation*, Zurich, Swtizerland (2010) pp. 15–17.
15. C. S. Gatla, R. Lumia, J. Wood and G. Starr, "An automated method to calibrate industrial robots using a virtual closed kinematic chain," *IEEE Trans. Robot.* **23**(6), 1105–1116 (2007).
16. J. H. Borm and C. H. Meng, "Determination of optimal measurement configurations for robot calibration based on observability measure," *Int. J. Robot. Res.* **10**(1), 51–63 (1991).
17. M. R. Driels and U. S. Pathre, "Significance of observation strategy on the design of robot calibration experiments," *J. Robot. Syst.* **7**(2), 197–223 (1990).
18. A. Nahvi, J. M. Hollerbach and V. Hayward, "Calibration of a Parallel Robot Using Multiple Kinematic Closed Loops," *Proceedings of the 1994 IEEE International Conference on Robotics and Automation*, San Diego, CA, USA (1994) pp. 407–412.
19. A. Nahvi and J. M. Hollerbach, "The Noise Amplification Index for Optimal Pose Selection in Robot Calibration," *Proceedings of the 1996 IEEE International conference on Robotics and Automation*, Minneapolis, MN, USA (1996) pp. 647–654.
20. H. Zhuang and Z. S. Roth, "Robot calibration using the CPC error model," *Robot. Comput.-Integr. Manuf.* **9**(3), 227–237 (1992).
21. H. Zhuang and Z. S. Roth, "Optimal design of robot accuracy compensators," *IEEE Trans. Robot. Autom.* **9**(6), 854–857 (1993).
22. J. L. Caenen and J. C. Angue, "Identification of Geometric and Nongeometric Parameters of Robots. Robotics and Automation," *Proceedings of the IEEE International Conference on Robotics and Automation*, Cincinnati, OH, USA (1990) pp. 1032–1037.
23. J. J. Craig, *Introduction to Robotics: Mechanics and Control* (Addison-Wesley, Boston, MA, 1986).
24. Y. Sun and J. M. Hollerbach,"Observability Index Selection for Robot Calibration," *Proceedings of the 2008 IEEE International Conference on Robotics and Automation*, Pasadena, CA, USA (2008) pp. 831–836.